Hypersonic Boundary-Layer Stability over Blunt Leading Edges with Bow-Shock Effects

Sean Hu *and Xiaolin Zhong †
University of California, Los Angeles, California 90095

Abstract

The stability of the hypersonic flow over a parabolic leading edge is numerically investigated using linear stability analysis accounting for the existance of shock waves in comparison with direct numerical simulations. The linear stability analysis is performed using a global spectral collocation method accounting for the shock effects by using Rankine-Hugoniot shock conditions on the upper boundary. It has been confirmed that the linear stability of the hypersonic flow between a bow shock and a parabolic leading edge has a new family of modes, namely shock modes, in addition to the first and higher modes found in the flat plate boundary layer case. The shock modes can be unstable at certain range of frequencies before the boundary layer first and higher modes begin to dominant. The stability characteristics of the shock modes and boundary layer modes are investigated. It is found that the shock modes and the first modes have rapid changes in their amplification rates when their wavenumbers cross. The effects of the Reynolds number are also investigated. Second and higher modes are found to be the dominant modes in the high Reynolds number case.

1 Introduction

The prediction of stability and transition of hypersonic flows is critical to the accurate calculations of aerodynamic forces and heating rates for hypersonic vehicles. For hypersonic flow over blunt bodies, many factors, such as bow shocks, surface curvature, entropy layer, nose bluntness, and real gas effects, influence the characteristics of hypersonic flow instability. Early experimental results on hypersonic transition include the work by Kendall [14] and Demetriades [4]. Stetson et al. [29] investigated the stability of the laminar boundary layer on a blunt, 7-degree half angle cone at $M_\infty = 8$ experimentally. It was found that small nosetip bluntness make significant changes in the stability characteristics of the boundary layer comparing to sharp cone. Namely, the critical Reynolds number in the case with small bluntness is found to be much higher than the case with a sharp cone. They also found that disturbances grow outside the boundary layer, in the entropy layer, indicating the existance of an inviscid instability. A series of theoretical and numerical work were conducted on the supersonic and hypersonic instability problems in comparison with the experimental results. Reshotko et al. [27] used a multiple scales method to analyze the spatial stability of a laminar supersonic flow over a blunt plate. Cowley et al. [3] investigated the instability of a compressible flow past a wedge in the hypersonic limit using asymptotic analysis. Several authors [22] [16] [8] [13] compared numerical linear stability results with Stetson's experimental results. They showed qualitative agreement with the experimental results. However, the spatial amplification rates of the second modes resolved by numerical approaches show much higher maxima than the experimental results. Kufner et al. [16] studied the effects of mean flow variations on the instability of hypersonic flow past blunt cones in resolving the discrepancies in the amplification rate. They found that the discrepencies were not due to the use of different mean flow solutions. Indeed, the discrepancies may due to the known limitations of the theoratical and numerical linear stability approaches as well as inaccurate main flow solutions.

Recently, direct numerical simulations (DNS) of hypersonic flow over a parabolic leading edge including the effects of boundary layers and shock layers were conducted by Zhong [36] who studied the generation of instability waves due to freestream acoustic disturbances for a two-dimensional Mach 15 flow over a parabola by numerically solving full Navier- Stokes equations using a new explicit fifth-order shock fitting upwind scheme. Better understanding of the stability characteristics of the hypersonic parabolic body flow can be achieved if the overall wave phenomena from DNS can be decomposed into linear and non-linear parts, and the effects of the shock wave, curvature, and three-dimensional waves can be identified. The numer-

---

[*] Graduate Student, seanh@seas.ucla.edu

[†] Assistant Professor, Mechanical and Aerospace Engineering Department, Member AIAA

ical linear stability tools have the flexibility to study the effects of curvature, shock boundary conditions, as well as wave angles. A comparison between the DNS and the linear stability (LST) results may provide insights to the stability characteristics of the flow.

Since the flow of interest is confined between the body surface and the bow shock, it is expected that both boundaries will affect the stability characteristics. The effects of the shock boundary conditions were evident from the DNS results. [35] Most of the research done before regarding the linear stability of the compressible flows, however, ignored the presence of a shock and used free stream (homogeneous) conditions at the far field or the asymptotic conditions just outside the boundary layer. For the hypersonic parabolic body case where important wave phenomena are observed between the viscous boundary layer and the shock, the shock plays a vital role and introduces additional flow features, such as entropy layer, to the flow. It is therefore reasonable to use appropriate shock boundary conditions instead for stability analysis.

It is known that there exist wave interactions among the shock wave, boundary-layer originated instability waves and the free stream disturbances for hypersonic flow instability. The theoretical approach in analyzing the problem was developed by Ribner [26] and McKenzie *et al.* [24] Anyiwo *et al.* [1] used this approach in analyzing the turbulence amplifications in the shock wave/boundary layer interaction. The main result of this theory is that the interaction of any mode, for instance, an acoustic wave with a shock wave, produces all three modes, an acoustic mode, a vorticity mode and an entropy mode. A recent study by Duck *et al.* [7] also led to similar conclusions. More recent approach of solving the problem involves direct numerical simulations. Zang *et al.* [33] examined the interaction of plane waves with shocks using the DNS approach and confirmed the linear theory results. In the aforementioned investigations, disturbances were considered to originate ahead of the shock. In the hypersonic parabolic body case, however, the disturbances come from behind the shock. The first attempt to study the effects of a shock on the boundary layer stability was probably Petrov's work [25]. In solving the compressible boundary layer linear stability problem, he replaced the inviscid asymptotic eigensolution outside the boundary layer by the linearized steady Rankine-Hugoniot condition for the normal momentum equation as the shock boundary condition. Insodoing, he obtained solutions for a two-dimensional flow over a wedge in the hypersonic limit. The triple-deck theory was used by Cowley *et al.* [3] along with the linearized Rankine-Hugoniot conditions to investigate the influence of a shock on the stability of boundary layer flow over a wedge. A key result obtained was that the presence of a shock allows more than one unstable viscous mode for relatively small ranges of frequency. Recently, Seddougui *et al.* [28] also found multiple viscous unstable modes in the linear stability analysis of hypersonic flow over a sharp slender cone with an attached shock using the triple-deck structure approach.

Chang *et al.* [2] started from the unsteady Rankine-Hugoniot conditions to obtain a set of perturbation equations accounting for the effect of shock velocity due to the perturbed wave originated from inside the boundary layer. This set of equations were then imposed as boundary conditions at the shock for the quasi-parallel linearized stability equations for compressible flows. They used a multidomain spectral method and a fourth order compact difference scheme to solve the stability equations. Their results showed that the shock has little effect on the boundary layer stability (subsonic first and second mode disturbances) when the shock is located outside the boundary layer edge. The presence of the shock induces unstable supersonic modes at finite Reynolds numbers which have oscillatory structure between the boundary layer and shock. When the shock is sufficiently close to the boundary layer edge, the shock influences the wave modes with finite disturbance amplitude near the shock. Stuckert [30] used similar approach as above in solving the linear stability problem for hypersonic flow over a sharp cone.

This paper studies the linear stability of hypersonic flow over a parabolic body in conjunction with DNS simulations. In the present study, the formulations of the temporal and spatial linear stability equations followed Malik [23] closely. The results for the spatial hypersonic parabolic body problem are mostly obtained using the spectral collocation method. Shock jump conditions are enforced following the formulation by Chang et al. [2] closely. To better approximate the physical conditions in the hypersonic parabolic body problem, in addition to the shock jump conditions, the basic flow normal velocity (V) terms are not neglected in the linear stability analysis. Linear stability results with shock jump condition for the hypersonic parabolic body problem are then presented along with DNS results with a focus on the fundamental wave phenomena. Specifically, LST results are used to identify the wave modes found in DNS. The stability characteristics of the important modes, including the effects of wall cooling, wave angle, and Reynolds number are also discussed.

2 Formulation

A. Governing Equations

The linear stability is considered for compressible viscous flow confined between two boundaries located at $y^* = 0$ (lower boundary) and $y^* = L^*$ (upper boundary), where the superscript "$*$" represents dimensional quantities. In the Cartesian coordinates, the x^*, y^*, z^* coordinates are those in the stream wise, wall-normal, and spanwise directions respectively. The gas is assumed to be a perfect Newtonian gas. The flow variables at the upper boundary (just behind the shock) are denoted by a subscript "e". In the case of hypersonic flow over parabolic bodys, the upper boundary is the shock wave, while the lower boundary is the body surface. The temperatures and velocities at the boundaries are computed together with the basic flow profiles. The full three-dimensional Navier-Stokes equations for compressible flow are used for the basic flow. The governing equations and the nondimensionalization details can be found in Ref. [11] The dimensionless variables are represented by the same symbols as those used for the dimensional variables but without the superscript "$*$". The Reynolds number is defined as

$$Re = \frac{U_e^* \rho_e^* L^*}{\mu_e^*}\,, \tag{1}$$

and the Mach number is

$$M_e = \frac{U_e^*}{(\gamma R^* T_e^*)^{\frac{1}{2}}}\,, \tag{2}$$

where $R^* = c_p^* - c_v^*$, c_v^* is the specific heat at constant volume, and $\gamma = 1.4$ is the ratio of specific heats. The Prandtl number is defined as $Pr = \mu^* c_p^* / k^*$ and is assumed to be 0.72.

B. Basic flow solutions

Basic flow solutions for the hypersonic flow over a parabolic leading edge was obtained by Zhong[35] by using a new high-order shock-fitting scheme. Note that the DNS and the linear stability analysis share the same high-accuracy basic flow solutions. Since the wave patterns are quite complex both close to the wall and to the shock, a natural choice of stretching function for the linear stability analysis is a cosine function. The basic flow at the collocation points are then obtained by using a high order interpolation scheme.

C. Linear stability equations

The linear stability analysis is based on a normal mode analysis of the linearized perturbation equations of the three-dimensional Navier-Stokes equations. The LST formulas presented in this paper are for general compressible flows with parallel steady flow fields. The perturbation equations are derived by representing the instantaneous flow variables as a sum of a basic flow solution and a small fluctuation quantity, i.e.

$$\begin{array}{rcl} u & = & \overline{U}(y) + u'(x,y,z,t) \\ v & = & \overline{V}(y) + v'(x,y,z,t) \\ w & = & w'(x,y,z,t) \\ p & = & \overline{p} + p'(x,y,z,t) \\ T & = & \overline{T}(y) + T'(x,y,z,t) \end{array} \quad . \tag{3}$$

Substituting Eq. (3) into the nondimensional form of the governing equations, and dropping the nonlinear and high-order terms yield a set of linear differential equations for the perturbation variables. Details of the linear perturbation equations and other formulations can be found in Malik.[23] In the normal mode analysis for the linear disturbances, the fluctuations of flow quantities are assumed to be represented by normal harmonic waves of the following form:

$$\begin{array}{l} [u',\, v',\, p',\, T',\, w']^{tr} = [\hat{u}(y),\, \hat{v}(y), \\ \hat{p}(y),\, \hat{T}(y),\, \hat{w}(y)]^{tr}\, e^{i\,(\alpha x + \beta z - \omega t)}\,, \end{array} \tag{4}$$

where α and β are the wavenumbers in x and z directions respectively, and ω is the frequency of the disturbance waves. These parameters are in general complex numbers. The complex amplitude eigenfunction of a typical flow variable, say u, is $\hat{u}(y)$. Substituting Eq. (4) into the linearized perturbation equations leads to a homogeneous system of ordinary differential equations:

$$(\mathbf{A}\, D^2 + \mathbf{B}\, D + \mathbf{C})\, \Phi = 0\,, \tag{5}$$

where D is the derivative operator in y direction, i.e., $D = d/dy$ and $D^2 = d^2/dy^2$. In the equation above, Φ is a vector defined as $\Phi = [\hat{u}(y), \hat{v}(y), \hat{p}(y), \hat{T}(y), \hat{w}(y)]^T$. **A**, **B** and **C**, which are 5×5 matrices, are functions of α, β, ω, Re, M_∞, and the basic flow solutions. The detailed expressions of matrices **A**, **B** and **C** can be found in Ref. [23], and they are not repeated here. In solving the linear stability problem for the hypersonic parabolic body case, where the normal direction basic flow velocity V is not very small comparing to U, it is reasonable to add the terms with V ignored by the parallel assumption back to matrices **A**, **B** and **C**. These extra terms can also be found in Ref. [11].

D. Linear stability boundary conditions

In hypersonic boundary layer stability problems, no-slip conditions apply at the body surface, i.e.,

$$\hat{u}(0) = \hat{v}(0) = \hat{w}(0) = \hat{T}(0) = 0\,. \qquad (6)$$

At the bow shock, shock conditions must hold. We followed the derivations from Chang [2] closely for the shock jump conditions. For a shock given by $y_0 = f(x, z, t)$ with the time averaged shock position $\overline{y}_0 = \overline{f}(x)$ and the local shock slope $a = tan\theta = d\overline{f}/dx$, the jump conditions across the shock are:

$$\frac{\partial f}{\partial t}[Q] + \frac{\partial f}{\partial x}[E] - [F] + \frac{\partial f}{\partial z}[G] = 0. \qquad (7)$$

Vectors Q, E, F, G are defined by

$$\begin{array}{rcl} Q & = & (\rho, \rho u, \rho v, \rho w, e)^{tr} \\ E & = & (\rho u, \rho u^2 + p, \rho uv, \rho uw, (e+p)u)^{tr} \\ F & = & (\rho v, \rho uv, \rho v^2 + p, \rho vw, (e+p)v)^{tr} \\ G & = & (\rho w, \rho uw, \rho vw, \rho w^2 + p, (e+p)w)^{tr} \end{array} ,(8)$$

where

$$e = \frac{p}{\gamma - 1} + \frac{1}{2}\rho(u^2 + v^2 + w^2). \qquad (9)$$

The jump of any quantity ϕ across the shock is denoted by

$$[\phi] = \phi_1 - \phi_2 \qquad (10)$$

where the subscripts 1 and 2 denotes the conditions ahead and behind the shock wave, respectively. Equation (8) is the unsteady Rankine-Hugoniot condition which governs the unsteady motion of a shock wave. The position function of the shock can be perturbed according to

$$f = \overline{f} + f'. \qquad (11)$$

We assume that Eq. (8) is valid at $y = \overline{f}$ since for small disturbances $|f'| << |\overline{f}|$. We also assume there is no disturbances ahead of the shock. The disturbances in the boundary layer or shock layer can not penetrate through the shock because the flow is supersonic outside the shock layer. A normal mode analysis to Eq(8) leads to

$$i(\alpha[\overline{E}] + \beta[\overline{G}] - \omega[\overline{Q}])\hat{f} + a[\hat{E}] - [\hat{F}] = 0 \qquad (12)$$

where harmonic wave forms are used in consistency with the linear stability equations. The complete descriptions of shock jump conditions can be found in Chang [2] and Hu [10].

E. Temporal and spatial global linear stability problems

The homogeneous equation system (5) along with proper boundary conditions form an eigenvalue problem. When a temporal linear stability problem is considered, a set of real-value α and β is given, ω is solved for as an eigenvalue problem given by Eqs. (5) and (6):

$$\omega = \omega(\alpha,\, \beta,\, Re,\, M_\infty)\,. \qquad (13)$$

Meanwhile, The amplitude of the disturbance modes, $[\hat{u}(y),\, \hat{v}(y),\, \hat{p}(y),\, \hat{T}(y),\, \hat{w}(y)]^{tr}$, is solved as an eigenfunction of the boundary value problem. The real part of ω, $Re\{\omega\}$, represents the frequency of the disturbance modes, while the imaginary part, $Im\{\omega\}$, represents the temporal amplification rate of the disturbances. When $Im\{\omega\}$ is greater, equal to, or smaller than 0, a disturbance mode is unstable with finite amplification, neutrally stable, or stable with finite damping, respectively. We also define a complex wave (phase) velocity c of the disturbance waves as $c = \omega/\alpha$. The disturbance waves are three dimensional in general. Two-dimensional disturbance modes correspond to a special case of $\beta = 0$.

In order to compare with the DNS results, spatial stability problem is solved in conjunction with the shock boundary conditions. In a spatial stability problem, real-valued ω and β are assumed. While α is the complex eigenvalue to be solved for. The real part of α, α_r, represents the spatial frequency of the disturbance modes, while the imaginary part, α_i, represents the spatial amplification rate of the disturbances. When $-\alpha_i$ is greater, equal to, or smaller than 0, a disturbance mode is unstable with finite amplification, neutrally stable, or stable with finite damping, respectively.

Two linear stability numerical codes have been developed, one uses the fourth-order finite-difference discritization method, and the other uses the spectral collocation discritization methods. The detailed descriptions of these two methods can be found in Hu *et al.*, [10] and will not be repeated here. Both methods are global eigenvalue methods providing all possible eigenmodes. Both methods can be used to solve for either the temporal or the spatial eigenvalue problems. For the temporal stability problem, discretizing Eq. (5) using the fourth-order finite-difference method or the spectral collocation method, along with the proper boundary conditions, leads to a matrix eigenvalue problem:

$$\mathbf{A}'\mathbf{\Phi} = \omega\,\mathbf{B}'\mathbf{\Phi}\,, \tag{14}$$

where ω is the eigenvalue. The whole eigenvalue spectrum and eigenfunctions can be obtained numerically by solving Eq. (14) using the QZ or QR eigenvalue algorithm of the IMSL computer subroutine library.

The spatial eigenvalue problem is nonlinear in the linear stability equation Eq. (5) due to the viscous $\hat{u}_{xx}$ terms. Malik [23] has shown that the spatial problem can be fairly accurately approximated by dropping the α^2 terms in the global eigenvalue calculations resulting a linear problem for α.

$$\mathbf{A}'\mathbf{\Phi} = \alpha\,\mathbf{B}'\mathbf{\Phi}\,, \tag{15}$$

More accurate spatial stability solutions can be obtained by using local iterative methods based on the global results. The spatial results shown in the following are the global method results. Gaster's transformation

$$\alpha_i = -\frac{\partial \alpha_r}{\partial \omega_r}\omega_i \tag{16}$$

can also be used to transfer the temporal stability results to the corresponding spatial stability results.

3 DNS of Hypersonic Flow

The direct numerical simulation approach studies the transitional boundary layers [15] by numerically solving the time-dependent three-dimensional Navier-Stokes equations for the temporally or spatially evolving instability waves. Such simulation requires that all relevant flow time and length scales are resolved by the numerical solutions using highly accurate numerical methods. One of the difficulties in hypersonic flow DNS is that high-order schemes are required for the direct simulations, however, high-order linear schemes can only be used for the spatial discretization of the equations in the flow fields without shock waves.

In Ref. [35], a new high-order (fifth and sixth order) upwind finite difference shock fitting method for the direct simulation of hypersonic flow with a strong bow shock and with stiff source terms is presented. There are three main aspects of the new method for hypersonic flow DNS: a new shock fitting formulation, new upwind high-order finite difference schemes, and the recently derived [34] third-order semi-implicit Runge-Kutta schemes. The review of other current DNS works, the details of the new method, and the results of evaluation of numerical accuracy of the new schemes can be found in Ref. [35].

The receptivity of hypersonic flows to free stream acoustic waves is investigated here as shown in a schematic Fig.1. In general, three dimensional unsteady flow should be considered in the DNS studies since the most unstable first mode in hypersonic boundary layers are oblique three-dimensional instability waves [17], though the most unstable second mode is two dimensional. Presently, only the two-dimensional instability waves in hypersonic boundary layers are considered as a first step of the DNS of three-dimensional hypersonic boundary layers over blunt bodies. The free stream disturbances are planar acoustic waves with a fixed frequency, and the body is a parabolic leading edge. The generation of disturbance waves in the boundary layer are studied based on the DNS results. The numerical accuracy of the DNS results for such hypersonic boundary layer receptivity have been evaluated by grid refinement studies and have been reported in Ref. [35]. These test results are not presented here. The detailed results and discussion regarding DNS can be found in Ref. [35]

4 Numerical Accuracy of LST Results

The two linear stability codes using the fourth-order finite-difference method and the spectral collocation method were first validated by comparing their solutions with those of Malik [23] for the linear stability of the flat-plate compressible boundary layer. The comparison of the present numerical codes with Malik's numerical schemes are fairly good. The details of the comparisons can be found in [12].

For the hypersonic parabolic body case, a grid refinement study is done locally at one station with 120 and 240 grid points. Table 2 shows the relative errors of the shock mode and the first mode when the number of the grid points of the basic flow solutions and LST analysis increases from 120 points to 240 points. The relative errors for the spatial frequency α_r of both modes are on the order of 10^{-10} while those for the amplification rate α_i are on the order of 10^{-6}. These results indicate that the basic flow solutions from DNS satisfy the LST requirement. They also suggest that LST calculations can be carried out with 120 grid points for the current case with reliable accuracy.

Gaster's transformation is also used to ensure the accuracy of both the temporal and spatial code. Since the spatial code solves for all the eigenvalues α_r, α_i for a given real ω, and the temporal code solves for all the eigenvalues ω_r, ω_i for a given real α, one can take one specific spatial mode from the spatial eigenvalue spectrum and use the real part of the mode α_r as the input for the temporal code to see if the corresponding ω_r is retrieved by the temporal code or vice versa. For example, at $\omega = 133649.4Hz$, the first mode from the spatial code is $\alpha_r = 30.704965$, and $\alpha_i = 0.17596984$. If one takes $\alpha = 30.704965$ for the temporal code, the resulted ω_r is only 0.04% away from the ω used in the temporal code. When a second order central difference formula is used to approximate the partial derivative in Gaster's transformation Eq. (16), with $\Delta\alpha$ being 0.1% of α, the resulted α_i from the temporal results is 14% from the spatial code. The error may be partly due to the fact that current global spatial code ignores the α^2 terms in the disturbance equations to reduce computational costs. The second order approximation may also be considered as a source of error. The dropping of the α^2 terms is justified as a fast way to solve for the global spatial spectra [23]. For very accurate spatial eigenvalue solutions, local shooting methods are recommanded. From the above example, one sees that the accuracy of the temporal and spatial codes is further verified with Gaster's tranformation.

5 Results

5.1 Flow conditions

The receptivity of a two-dimensional boundary layer to weak freestream acoustic disturbance waves for a Mach 15 hypersonic flow past a parabolic leading edge at zero angle of attack are considered. In the DNS simulation, the freestream disturbances with fixed frequencies are superimposed on the steady basic flow to investigate the development of waves in the boundary layer with the effects of the bow shock interaction. The body surface is a parabola given by

$$x^* = b^* y^{*2} - d^*, \tag{17}$$

where b^* is a given constant and d^* is the reference length. The body surface is assumed to be a non-slip wall with an isothermal wall temperature $T_w{}^*$. A schemetic of the flow is shown in Fig. 1. The free stream flow conditions are:

$$\begin{aligned} &M_f = 15,\ T_f{}^* = 192.989K,\ T_w{}^* = 1000K,\\ &T_r{}^* = 288K,\ b^* = 40m^{-1},\ d^* = 0.1m,\\ &\mu^* = 0.1784 \times 10^{-4} kg/ms,\\ &Re_f = \rho_\infty{}^* U_f{}^* d^* / \mu_f{}^* = 6026.55. \end{aligned} \tag{18}$$

Note that low Reynolds numbers are chosen so that effective DNS simulations can be conducted. The linear stability analysis shares the same basic flow solutions with the DNS simulation. Since the linear stability analysis has to be conducted station by station, the nondimensionalization is done with respect to local shock layer edge values. The Reynolds number used in the calculations is the local Reynolds number R based on the local length scale. A more standard length scale $\delta(s)$ is used to scale the wave numbers and frequencies. $\delta(s)$ is defined as

$$\delta = \sqrt{\frac{s\nu_e}{U_e}} \tag{19}$$

where s is the distance from the leading edge as seen in Fig.1. The Reynolds number based on this length scale δ is R. A non-dimensional frequency F is also introduced which is difined as

$$F = \frac{\omega^* \nu^*}{U_f^{*2}} = \omega / Re_f\ . \tag{20}$$

A list of local flow parameters, including R, shock distance, and U_e corresponding to the station number, are given in Table 1.

5.2 LST and DNS comparisons

Due to the local nature of LST, comparisons of the disturbance eigenfunctions between LST and DNS results have to be made locally at each stations. Since the linear stability codes invoke parallel flow assumption (except regarding V terms), the body curvature and the pressure gradient which exist in DNS are ignored in the current analysis. Figure 2 shows the basic flow velocity and pressure profiles in the local wall-normal direction at various locations. The normal velocity V, shown as u_n in the figure, is about 10% of the streamwise velocity. Therefore, in the linear stability calculation, V and its associated terms are not ignored. A favorable pressure gradient is clearly present in the flow as opposed to the constant pressure assumption made in the LST codes. It is also seen that the pressure profiles approach that of the flat plate boundary layer further downstream. $\rho(du/dy)$ profiles are shown in the bottom figure of Fig. 2. The generalized inflection points do exist in the flow.

A common forcing frequency is enforced in DNS. This frequency is also enforced locally at each stations in the linear stability analysis. Although a range of forcing frequency is studied with LST, comparisons with DNS are made at two forcing frequencies, $F = 2655$, and $0.2F$. The DNS disturbance fields visualized with instantaneous contours of $Re\{v\}'$ for the two cases are shown in Figs. 3 and 4 respectively. For the high forcing frenquency case, the corresponding spatial frequency is relatively high. Similarly, the corresponding spatial frequency is low for the $0.2F$ case. Previously, some comparisons between DNS and LST were done for the $F = 2655$ case [11]. The focus of current work is the $F = 531$ case.

The basic flow solutions from DNS indicate that the local streamwise velocity profiles deviate from the flat plate boundary layer case especially close to the shock. For conveniance, the bacis flow close to the wall is refered to as the boundary layer and that close to the shock the shock layer. The pressure and velocity disturbance p' and u' are chosen to be the parameter of comparisons between DNS and LST. The DNS disturbance fields, shown in $Re\{\hat{v}'\}$ contours in Figs.3 and 4 indicate that there are at least two distinctive wave patterns in the flow field. One pattern matches with the boundary layer modes which originate from the boundary layer and propagate along the wall. The other pattern is quite new and represents wave propagation close to the bow shock. Notice that the waves propagating close to the shock wave form certain angles with respect to the body surface.

The eigenvalues and eigenfunctions of the disturbances at each stations are the LST results. Figure 5 shows a typical spatial eigenvalue spectrum at station 14 with $R = 143.04$ and $F = 531$. The spectrum without shock boundary conditions is also shown. There are two distinctive families of modes in the spatial spectrum. Modes in the lower left branch correspond to the boundary layer modes, including first, second and higher modes. Their eigenfunctions $Re\{\hat{p}\}$ and $Im\{\hat{p}\}$ for the first three modes are shown in Fig. 6. The unstable mode $\alpha_r = 31.201271, \alpha_i = -0.076501078$ is the first mode, and is the right most mode in the left branch. Similarly, the lower right branch modes, including the least stable mode, which is just to the right of the first mode with $\alpha_r = 32.032739, \alpha_i = 0.002061067$, seem to have distinctive features in the shock layer, are named shock layer modes. The eigenfunctions for the first three shock layer modes are shown in Fig. 7. It is found that depends on the forcing frequency and the Reynolds number, the dominant boundary layer modes can be the first modes, the second modes and higher modes. In the cases studied so far, the only unstable shock family modes are the shock modes. Notice that eigenfunctions of the boundary layer modes for this flow deviate from those for the flat plate boundary layer case in the shock layer. This deviation is however expected.

For the case of $F = 531$, the evolutions of shock modes, first modes and higher modes take place in a much longer region in the streamwise direction than the $F = 2655$ case. In the mean time, the development of the boundary layer modes in the normal direction is affected more by the shock. Figures 8, 9 and 10 show the evolution of disturbances in $|\hat{p}|$ from DNS in comparison with the shock modes and the first modes. The wavenumbers and amplification rates of the shock modes and the first modes are close to the disturbance resolved by DNS. Therefore, only these modes are compared with the DNS results. In each of the three figures, the DNS results are shown in the top row. The shock mode eigenfunctions are shown in the middle row, whilst the first mode eigenfunctions bottom row. In Fig. 8, the results at stations 1,3,5,7,and 9 are compared. The first mode eigenfunctions at station 1 and 3 are not shown because they are very stable comparing to the DNS results and the shock modes. The initial comparisons at stations 1,3, and 5 are clearly not good. This is due to the fact that the receptivity and the initial growth, which are observed experimentally and resolved by DNS, can not be addressed with LST. In fact, close to the leading edge, due to the different natare of the basic flow, the linear stability equations can no longer represent the physical stability mechanism properly. At stations 5 and 7, the LST shock modes start to agree with the DNS results qualitatively. This trend becomes more clear at station 11 shown in Fig. 9. Figure 9 shows the results from station 11 to 19. At stations 11, 13, and 15, the DNS results show a change of dominant modes from the shock modes to the first modes. First mode signiture starts to develope in the shock mode region. From station 15 on, including the stations 21 to 29 shown in Fig. 10, it is quite clear that the first modes are the dominant modes from the DNS results. However, there is still shock mode influence on each station. Notice that at station 17, the eigenfunction of the shock mode show a dramatic deviation from those at the neighboring stations. This phenomenon is not yet well understood and is associated with the wavenumber crossing effects discussed later.

Good comparisons in eigenfunctions are obtained in the region away from the leading edge where receptivity, curvature and the strong initial growth of the waves have lesser effects. They are shown in Figs.11 and 12, where the magnitude profiles of streamwise velocity and pressure disturbance of the first mode are compared at station 19, $R = 179.38, F = 531$. Indeed, the first modes are unstable at certain stations at this frequency and remain the dominant modes close to the wall. Another example is shown in Figs. 13 and 14 at station 21 with $R = 192.54$. To compare the wavenumbers of the DNS results with the LST results, a wavenumber evaluation scheme is used to extract the wavenumber from the DNS surface entropy data. The determination of the wavenumber is based on the fact that waves propagate with linear phase in the streamwise direction and a 360° phase change corresponds to a propagation of one wave length. The results are compared with LST first mode, second mode and shock mode wavenumbers in Fig.15. It can be seen that at the initial stage, the wavenumber from DNS experience a sharp increase. Linear stability analysis is conducted away from the initial region. Away from the initial region, the wavenumber of the first mode match closely with the DNS wavenumber at the wall. The wavenumber of the shock modes from LST is also close to that of the first modes. This can be observed graphically from the DNS disturbance field shown in Fig. 4 which indicates that the wave pattern close to the shock has roughly the same wavenumber as that close to the wall. This agreement provides us a nessesary condition for the eigenfunction comparisons shown in the previous figures. The amplification rate path comparison is shown in Fig. 16. The DNS amplification rate is evaluated at the wall with a third order scheme. The poor comparison can be attributed to the strong initial growth of the disturbance waves captured by DNS which agrees with the experimental observations. LST, however, cannot predict this phenomenon. Nontheless, the amplification rate path of different modes from LST is further shown in Fig.17. It is clear that LST predicts the change of dominance of the boundary layer modes in the streamwise direction from the first modes to higher modes. Under the current situation, the flow field is quite stable except for a short range where the first modes become unstable.

5.3 Stability characteristics

It has been shown so far that both LST and DNS resolve boundary layer modes and shock layer modes. However, the stability characteristics of these modes, especially how the boundary layer modes are modified under the current flow conditions, are not yet known. Specifically, the effects of wave angle, wall-cooling, forcing frequency, and Reynolds number are investigated.

A. Wave angle effects

The effects of wave angle can be studied locally keeping the magnitude of the wavenumber vector $\mid \vec{k} \mid$ constant. Therefore, three-dimensional Gaster's transformation is used to transform the temporal stability results to the spatial stability results. Figure 18 illustrates the effects of wave angle on shock modes, first and second modes. The wave angle effect result is shown at station 21, $R = 192.54$. The first mode is initially stable with 0° wave angle. Its amplification rate $-\alpha_i$ increases with wave angle and peaks out at around 55° where it already is unstable. The second mode however, is clearly two-dimensional since the amplification rate decreases with wave angle. The change of the amplification rate for the shock modes are very small comparing to that for the boundary layer modes. The wave angle effects for the boundary layer modes are similar to the well known results of the flat plate boundary layer modes. An alternative way to study the effects of wave angle is to follow the wave modes traveling with different wave angles downstream while keeping the forcing frequency F constant. The results for the first modes at $F = 531$ is shown in Fig. 19. It is clear that initially three-dimensional waves propagate with higher amplification rates. However, the amplification rates of waves with large propagating angle quickly start decaying in the streamwise direction, leaving the least stable mode to be the two-dimensional modes downstream. The results seem to be inconsistant with the previous observation. The inconsistancy can be explained by Fig. 20 where the magnitude of the wavenumber vector $\mid \vec{k} \mid$ corresponding to the waves shown in Fig. 19 is shown. The magnitude of the wavenumber vector $\mid \vec{k} \mid$ increases in the streamwise direction under current situation which is a more realistic situation for studying the three-dimensional effects.

B. Wall-cooling effects

It is well known that for compressible flow flat plate boundary layer, the first modes are stabilized with wall-cooling while the second modes are distablized with wall-cooling. For the hypersonic parabolic body case, in the range of Reynolds number and frequency studied, the shock modes and the first modes are the more important modes. Therefore, the effects of wall-cooling are investigated for those modes. A set of basic flow solution with higher surface temperature is used for comparison. Comparison is made at station 12, with $F = 531$. Due to the fact that the change of surface temperature affects other flow parameters, the basic flow parameters resulted from different surface temperature, such as Mach number, streamwise velocity behind the shock, and shock distance are only close but not identical. Nonetheless, the impact of cooling the surface can be seen with the comparison. For the low surface temperature case, the ratio between the surface temperature and the temerature behind the shock is 0.60. While in the high surface temperature case, the ratio is 1.18. The temperatures behind the shock at station 12 differ 1.8% in two cases. The difference in streamwise velocity at the same location is 0.3%. Figure 21 shows that dramatically different surface temperature does not alter the wavenumber of the first modes much. Nonetheless wall-cooling does stablize the three-dimensional first modes. As for the shock modes, the cooled wall also stabilizes the shock mode, but has very little effect on the wavenumber of the shock mode. This is shown in Fig. 22.

C. Effects of forcing frequency

It is found that shock modes can be unstable before the first modes get amplified in certain range of forcing frequency. This phenomenon is studied with some detail. Figure 23 shows the wavenumber and the amplification rate of the first modes and the shock modes at station 9 over a range of frequency normalized by $\omega_0 = 668247 Hz$ ($F = 2655$). The upper figure shows that the wavenumbers of the first mode and the shock mode cross at around $\omega^* = 0.32$. When the wavenumbers cross, the amplification rate of the shock mode change quite rapidly from almost a flat line to a peak followed by a valley. While almost the exact reverse happens to the first mode amplification rate. Similar rapid changes occur at other stations when the wavenumbers of the first modes and the shock modes come close. At station 10, as shown in Fig. 24, this rapid change even brings first modes to be unstable allowing two unstable modes at $\omega^* = 0.29$. Unstable first modes due to this mechanism, however, are only found at station 10. The first modes become "systematically" unstable starting from station 13. This rapid change in amplification rate associated with the crossing of wavenumbers between the shock modes and the first modes is not yet well understood at this stage. Although this phenomenon has not been mentioned in the flat plate boundary layer linear stability study, it has been found to exist in the case of compressible viscous Couette flow. Hu et al. [12] found that in viscous Couette flow case, at certain Mach numbers. the inviscidly stable mode I can be unstable when the its wavenumber cross with some viscous mode. This crossing of the wavenumbers similarly triggers rapid changes in the amplification rate of both the mode I and the viscous mode which is shown in Fig. 25 at Mach 2.7 in the temporal stability context where ω_i vs. α plot is equavalent to $-\alpha_i$ vs. ω plot shown in Fig. 23. This phenomenon, though yet to be understood, might have a significant impact on the transition scenario of the hypersonic parabolic body problem since this may cause a fundamental resonance to take place early.

D. Stability contours

The effects of Reynolds number and forcing frequency on the stability of the shock modes and the first modes are illustrated in Fig. 26 with the stability contours for the shock modes and the first modes drawn against Reynolds number R and non-dimensional frequency F. The spotty unstable first modes associated with wavenumber crossing mentioned earlier are not shown in the contour for clarity. In general, the shock modes are dominant in the early stage before the first modes take over. The shock mode instability region has an upper limit in forcing frequency of approximately $F = 1200$, while the first mode unstable region has an upper limit of approximately $F = 680$. The critical Reynolds number for the first modes is considerablely smaller in the current case than that in the flat plate boundary layer case due to different basic flow. The neutral curve of the first modes has two peaks as opposed to only one for the flat plate boundary layer first modes. The first modes are generally more unstable at lower frequency which implys that the effect of the bow shock close to the body surface is distablizing since at lower frequency, the disturbance waves travel with large wavelength and thus are affected more by the shock layer. The change of amplification rate of the shock mode with forcing frequency at various stations provides a clear picture of the cause of the unstable shock modes. This is shown in Fig. 27. There is one peak in amplification rate at each station corresponding to one wavenumber crossing mentioned earlier. The peaks are the source of the unstable shock modes. At station 11, the peak is not high enough to provide unstable modes. Therefore, the shock modes become stable at around $R = 118.14$.

Since both the shock modes and the first modes can be unstable, their categorization is investigated. In the frequency range studied, both modes are found to be subsonic modes. The relative Mach number, defined as:

$$\hat{M} = \frac{u - c_r}{\sqrt{T}} M_e, \tag{21}$$

where M_e stands for the Mach number just behind the shock, is ploted at station 13 for the first mode as shown in Fig. 28. Also shown in the figure is the first mode wave pattern along with the sonic line. According to the inviscid compressible stability theory, the inviscid unstable first modes correspond to a generalized inflection point in the basic flow. When the basic flow at station 13, where an unstable first mode is found, is checked, no inflection points are found.

E. Effects of Reynolds number and nose bluntness

To study the effects of Reynolds number and nose bluntness, a set of basic flow solution with the body geometry enlarged by 10 times is obtained with DNS. The reference length scale is increased from $l = 0.1m$ to $l = 1m$. The grid distribution is kept the same in the computations allowing station by station comparisons of LST results. All other flow conditions are the same. The result is an increase in Reynolds number based on δ of about $\sqrt{10}$ times locally. The LST results at the same grid points at this geometry are compared with the previous case. The comparisons are done at $F = 531$ for the shock modes first. Figures 29 and 30 are the comparisons of the wavenumber and the amplification rate of the shock modes at the first 11 stations. The high Reynolds number basic flow does not result in very different wavenumbers for the shock modes. However, the unstable shock modes observed in the previous case at the early stations do not exist for $F = 531$. The unstable or least stable boundary layer modes at each station for the higher Reynolds number case is plotted in Fig. 31 for $F = 531$. At the same frequency, the lower Reybolds number case does not have any unstable boundary layer modes in the corresponding region. For the higher Reynolds number case, there are two peaks in the amplification rate curve. The first unstable peak corresponds to the second modes while the second unstable peak corresponds to the third modes. This is illustrated in Fig. 32 where eigenfunctions $Re\{\hat{p}\}$ and $Im\{\hat{p}\}$ of the unstable modes at station 5 and 6 (first peak) and station 10 (second peak) are compared. Except for the modification by the shock layer, the eigenfunctions show that the second and third boundary layer modes are the unstable modes according to Mack's theory [18].

6 Conclusion

Comparisons of the stability results from LST and DNS are made for the hypersonic parabolic body flow. It is shown that the LST provides individual wave modes with close resemblances to the DNS solutions away from the leading edge. Specifically, these modes include the shock modes, the boundary layer first modes, second and higher modes. It is shown that the eigenfunctions of the shock modes and boundary layer modes take turn to match with the DNS results. Therefore, it is confirmed that there do exist shock modes which can be unstable before the boundary layer modes start to dominate. The influence of the shock modes die down downstream. Very close to leading edge, DNS and LST do not compare well as expected. The effects of wave angle are studied for the important modes. The first boundary layer modes are found to be most unstable when they are three-dimensional, and the second modes are two-dimensional. Walling cooling is found to stabilize the first modes and have very litte effects on the shock modes. These results match with the compressible linear stability theory. Lower forcing frequencies are found to cause instability in the flow. At $F = 1200$ and below, shock modes are found to be unstable initially. This instability is associated with the cross of wavenumbers of the first modes and the second modes and is not yet well understood. The first modes are also found to be unstable in the low frequency range ($F < 700$). The critical Reynolds number for the shock mode instability is around 120. Systematic linear stability study on higher Reynolds number has not been carried out. Current results show that higher Reynolds number leads to unstable second and third modes.

7 Acknowledgements

This research was supported by the Air Force Office of Scientific Research under grant numbers F49620-97-1-0030 and F49620-95-1-0405 monitored by Dr. Len Sakell.

References

[1] J. C. Anyiwo, D. M. Bushnell, "Turbulence amplification in shock-wave boundary-layer interaction," AIAA Journal,Vol.20, No.7,pp.893-899,1982.

[2] C. L. Chang, M. .R. Malik, "Effects of shock on the stability of hypersonic boundary layers," AIAA paper 90-01448, 1997.

[3] S. Cowley, P. Hall, "On the stability of hypersonic flow past a wedge," ICASE Report 88-72.,1988.

[4] A. Demetriades, "Laminar boundary layer stability measurements at Mach 7 including wall temperature effects," AFOSR-TR-77-1311, Nov. (1977).

[5] P. G. Drazin and W. H. Reid, *Hydrodynamic Stability*, Cambridge University Press, 1981.

[6] P. M. Duck, G. Erlebacher, and M. Y. Hussaini, "On the linear stability of compressible plane Couette flow," J. Fluid Mech., 258, 131-165 (1994).

[7] P. M. Duck, D. C. Lasseigne, and M. Y. Hussaini, "On the interaction between the shock wave attached to a wedge and freestream disturbances," Theoretical and Computational Fluid Dynamics, 7, 119-139 (1995).

[8] V. Esfahanian, "Computation and stability analysis of laminar flow over a blunt cone in hypersonic flow," Dissertation Ohio State University, 1991.

[9] M. C. Fischer, L. M. Weinstein, "Cone transitional boundary-layer structure at $M_e = 14$," AIAA Journal,Vol.10, No.5,pp.699-701, May 1972.

[10] S. H. Hu, X. Zhong, "Linear stability of supersonic plane Couette flow," AIAA paper 97-0432, 1997.

[11] S. H. Hu, X. Zhong, "Linear statbility of hypersonic flow over a parabolic leading edge," AIAA paper 97-2015, 1997.

[12] S. H. Hu, X. Zhong, "Linear stability of viscous supersonic plane Couette flow," To appear in Physics of Fluids, 1998.

[13] H. B.Johnson, G. V. Candler "Numerical study of hypersonic boundary layer transition on a blunt body," AIAA paper 97-0554, 1997.

[14] J. M. Kendall, "Wind tunnel experiments relating to supersonic and hypersonic boundary layer transition," AIAA Journal, 13(3), 290-299 (1975).

[15] L. Kleiser, T. A. Zang, "Numerical simulation of transition in wall-bounded shear flows," Ann. Rev. Fluid Mech., 23,495-535,1991.

[16] E. Kufner, U. Dallmann, J. Stilla, "Instability of hypersonic flow past blunt cones - effects of mean flow variations," AIAA paper No. 93-2983, January 1993.

[17] L. M. Mack, "Linear stability theory and the problem of supersonic boundary-layer transition," AIAA Journal, 13(3), 278-289 (1975).

[18] L. M. Mack, "Boundary-layer linear stability theory," AGARD Rep. 704, 3-1, 1984.

[19] L. M. Mack, "Review of linear compressible stability theory," in it Stability of Time Dependent and Spatially Varying Flows, edited by D. L. Dwoyer and M. Y. Hussaini, Springer-Verlag, 1987, pp. 164-187.

[20] L. M. Mack, "On the inviscid acoustic-mode instability of supersonic shear flows, part 1: two-dimensional waves," Theoretical and Computational Fluid Dynamics, 2, 97-123 (1990).

[21] M. R. Malik and S. A. Orzag, "Efficient computation of the stability of three-dimensional compressible boundary layers," AIAA paper No. 81-1277, 1981.

[22] M. R.Malik, R.E.Spall, C.-L.Chang, "Effects of nose bluntness on boundary layer stability and transition," AIAA paper No. 90-1112, January 1990.

[23] M. R. Malik "Numerical methods for hypersonic boundary layer stability," Journal of Computational Physics, 86,376-413 (1990).

[24] J. F. McKenzie, K. O. Westphal, "Interaction of linear waves with oblique shock waves," Physics of Fluids, Vol.11, No. 11, pp.2350-62, 1968.

[25] G. V. Petrov, "Stability of a thin viscous layer on a wedge in hypersonic flow of a perfect gas," in Laminar-Turbulent Transision, edited by V. V. Kozlov. Proceedings of 2nd IUTAM Symposium, Springer. 1984.

[26] H. S. Ribner, "Convection of a pattern of vorticity through a shock wave," NACA Rept. 1164,1954.

[27] E. Reshotko, M. M. S. Khan, "Stability of the laminar boundary layer on a blunted plate in supersonic flow," presented at IUTAM Symposium on Laminar-Turbulent Transition, Stuttgart, F.R.G.,Sept 1979.

[28] S. O. Seddougui, A. P. Bassom, "Instability of hypersonic flow over a cone," J. Fluid Mech., 345, 383-411 (1997).

[29] K. F. Stetson, E. R. Donaldson, J. C. Donaldson, L. G. Siler, "Laminar boundary layer stability experiments on a cone at Mach 8,Part 2: blunt cone," AIAA paper No. 84-0006, January 1984.

[30] G. K.Stuckert, "Linear stability theory of hypersonic,chemically reacting viscous flow," PhD dissertation, Arizona State University, 1988.

[31] C. K. W. Tam and F. Q. Hu, "On the three families of instability waves of high-speed jets," Journal of Fluid Mechanics, 201, 447–483 (1989).

[32] C. K. W. Tam and F. Q. Hu, "The instability and acoustic wave modes of supersonic mixing layers inside a rectangular channel," Journal of Fluid Mechanics, 203, 51–76 (1989).

[33] T. A. Zang, M. Y. Hussaini, and D. M. Bushnell, "Numerical computations of turbulence amplification in shock-wave interactions," AIAA Journal,Vol.22, No.1,pp.12-21,1984.

[34] X. Zhong, "Additive semi-implicit Runge-Kutta schemes for computing high-speed nonequilibrium reactive flows," Journal of Computational Physics, 128, 19-31 (1996).

[35] X. Zhong, "Direct numerical simulation of hypersonic boundary layer transition over blunt leading edges, part I: A new numerical method and validation," AIAA paper 97-0755, 1997.

[36] X. Zhong, "Direct numerical simulation of hypersonic boundary layer transition over blunt leading edges, part II: A new numerical method and validation," AIAA paper 97-0756, 1997.

[37] M. Zhuang, P. E. Dimotakis, and T. Kubota, "The effect of wall on a spatially growing supersonic shear layer," Physics of Fluids A, 2(4), 599-604 (1990).

Table 1: Flow properties by station for hypersonic flow over parabolic body.

Station	δ	R	Shock Distance	U_e
1	0.1060285E-02	34.145498333	0.17864E-01	2900.4881
2	0.1134150E-02	41.002348016	0.21903E-01	3066.9497
3	0.1207434E-02	48.016105688	0.26279E-01	3195.7327
4	0.1281194E-02	55.296790562	0.31038E-01	3299.7828
5	0.1356168E-02	62.922465807	0.36229E-01	3386.3814
6	0.1432859E-02	70.949308595	0.41894E-01	3459.9652
7	0.1511610E-02	79.417556280	0.48074E-01	3523.4246
8	0.1592649E-02	88.355371970	0.54806E-01	3578.7519
9	0.1676125E-02	97.781544440	0.62122E-01	3627.3883
10	0.1762134E-02	107.70747220	0.70053E-01	3670.4195
11	0.1850737E-02	118.13867030	0.78626E-01	3708.6905
12	0.1922085E-02	126.67682581	0.85818E-01	3735.8289
13	0.1990920E-02	135.02017330	0.92994E-01	3759.3836
14	0.2056367E-02	143.04116600	0.100026485	3779.7092
15	0.2118879E-02	150.77592664	0.106929937	3797.4740
16	0.2178818E-02	158.25403455	0.113716309	3813.1678
17	0.2236479E-02	165.50010326	0.120395652	3827.1596
18	0.2292106E-02	172.53489603	0.126976565	3839.7324
19	0.2345903E-02	179.37613534	0.133466489	3851.1081
20	0.2398043E-02	186.03910378	0.139871914	3861.4630
21	0.2448674E-02	192.53709890	0.146198544	3870.9390
22	0.2497923E-02	198.88178336	0.152451433	3879.6524
23	0.2545901E-02	205.08345865	0.158635081	3887.6987
24	0.2592705E-02	211.15128194	0.164753519	3895.1580
25	0.2638420E-02	217.09343998	0.170810379	3902.0972
26	0.2683123E-02	222.91729005	0.176808946	3908.5733
27	0.2726880E-02	228.62947531	0.182752205	3914.6350
28	0.2769753E-02	234.23602015	0.188642877	3920.3239
29	0.2811796E-02	239.74240952	0.194483456	3925.6763
30	0.2853058E-02	245.15365556	0.200276231	3930.7235

Table 2: Grid refinement evaluation on LST results. Station 1,$R = 34.15$.

Basic flow N	Shock mode α_r	Relative Error	Shock mode α_i	Relative Error
121	160.544537666	$1.68E-10$	0.082557611	$2.42E-6$
241	160.544537639	–	0.082557411	–
Basic flow N	First mode α_r	Relative Error	First mode α_i	Relative Error
121	178.953356383	$2.43E-6$	3.989141765	$3.66E-6$
241	178.952921072	–	3.989156350	–

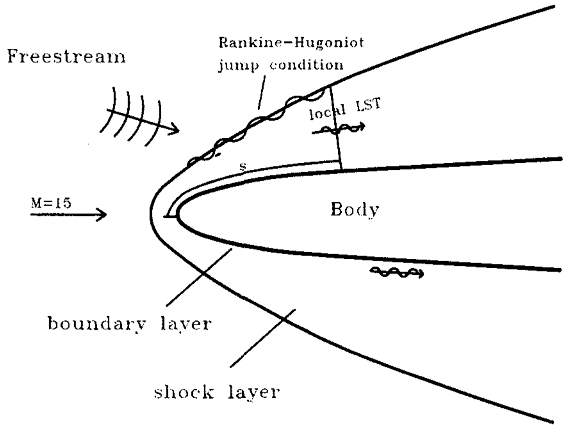

Figure 1: A schematic of Mach 15 hypersonic flow over a parabolic leading edge. s is the local surface distance from the leading edge, and is used for Reynolds number R.

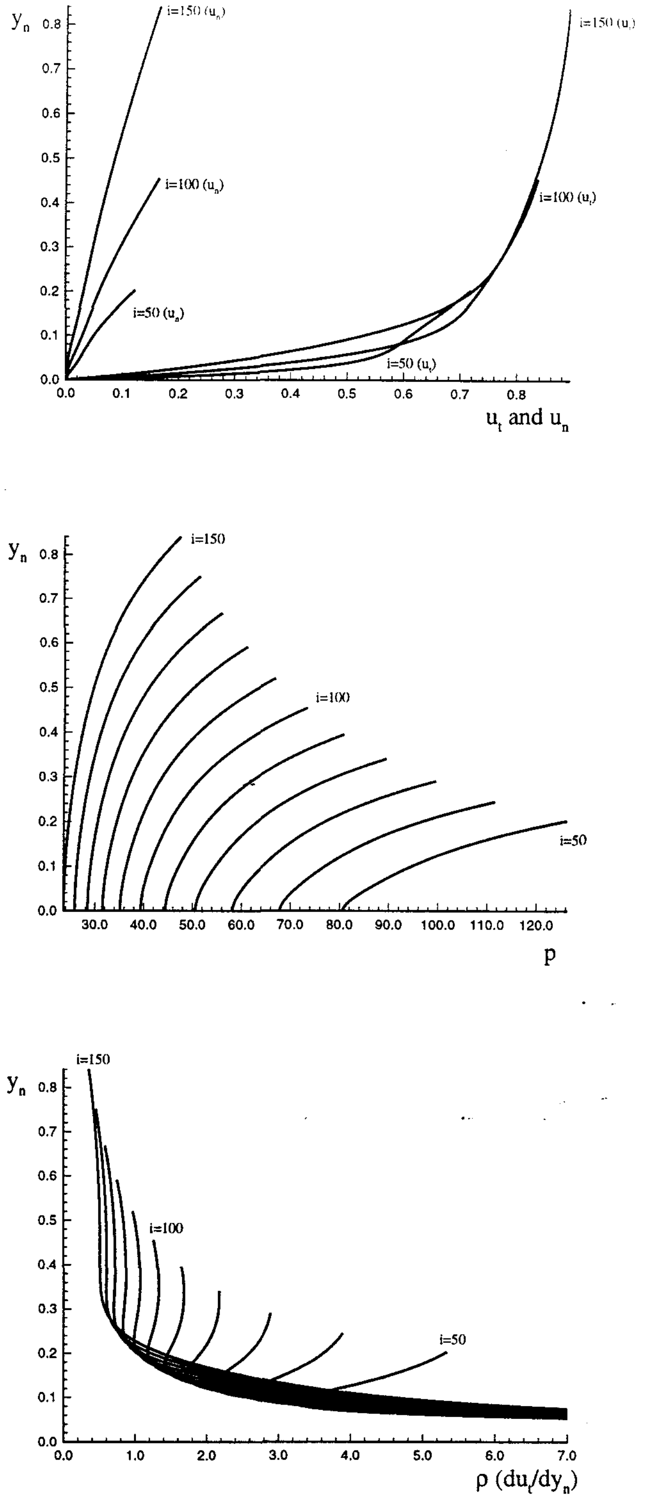

Figure 2: Basic flow streamwise velocity (upper), pressure (middle), and $\rho(du/dy)$ (lower) profiles in the wall normal direction at various streamwise locations. $\rho(du/dy)$ profiles are related to the generalized inflection points.

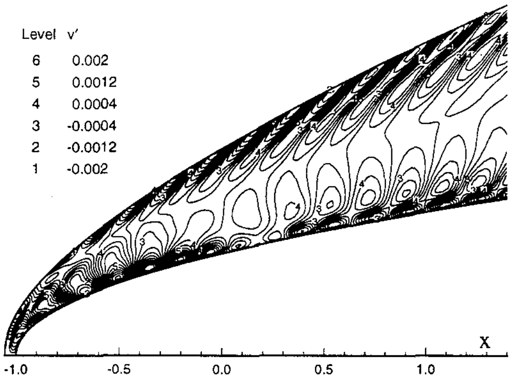

Figure 3: The DNS results of instantaneous contours instantaneous v'.

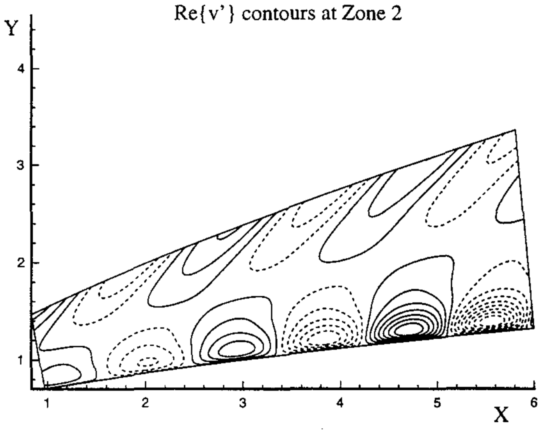

Figure 4: The DNS wave patterns visualized with $Re\{\hat{v}'\}$ at $F = 531$ from station 11 to station 29.

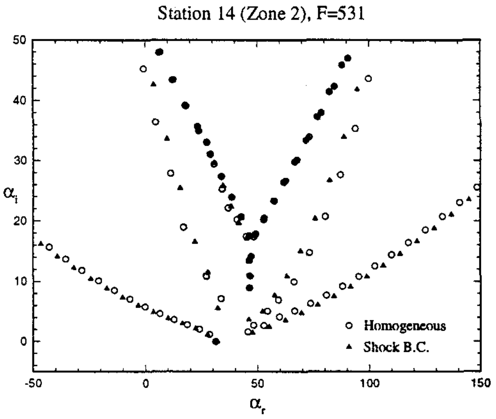

Figure 5: The LST eigenvalue spectra at Station 14, $R = 143.04, F = 531$ with homogeneous shock conditions and shock jump conditions.

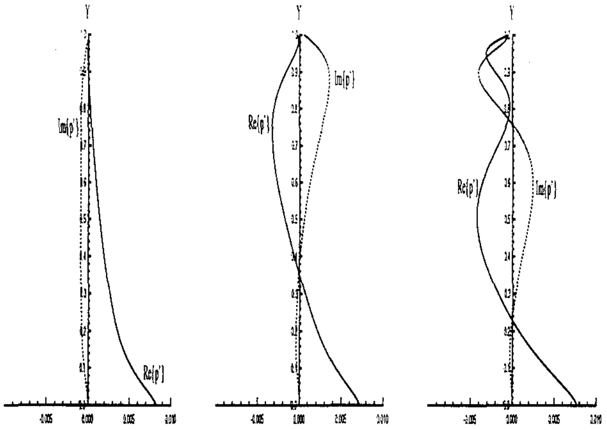

Figure 6: The eigenfunctions of the boundary layer modes at Station 14, $R = 143.04, F = 531$ with shock jump conditions. Left figure, first mode. Middle figure, second mode. Right figure, third mode.

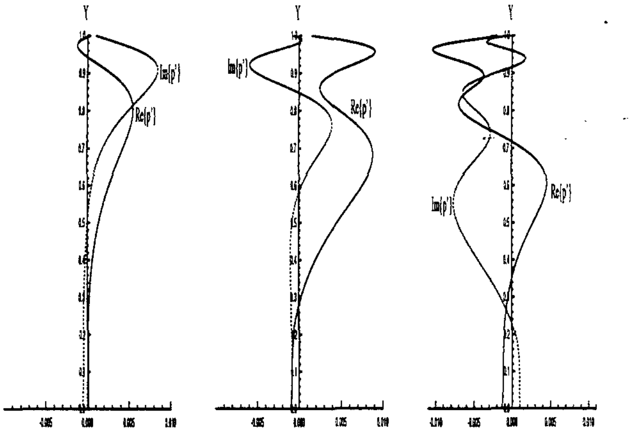

Figure 7: The eigenfunctions of the shock layer modes at Station 14, $R = 143.04, F = 531$ with shock jump conditions. Left figure, shock mode. Middle figure, second shock layer mode. Right figure, third shock layer mode.

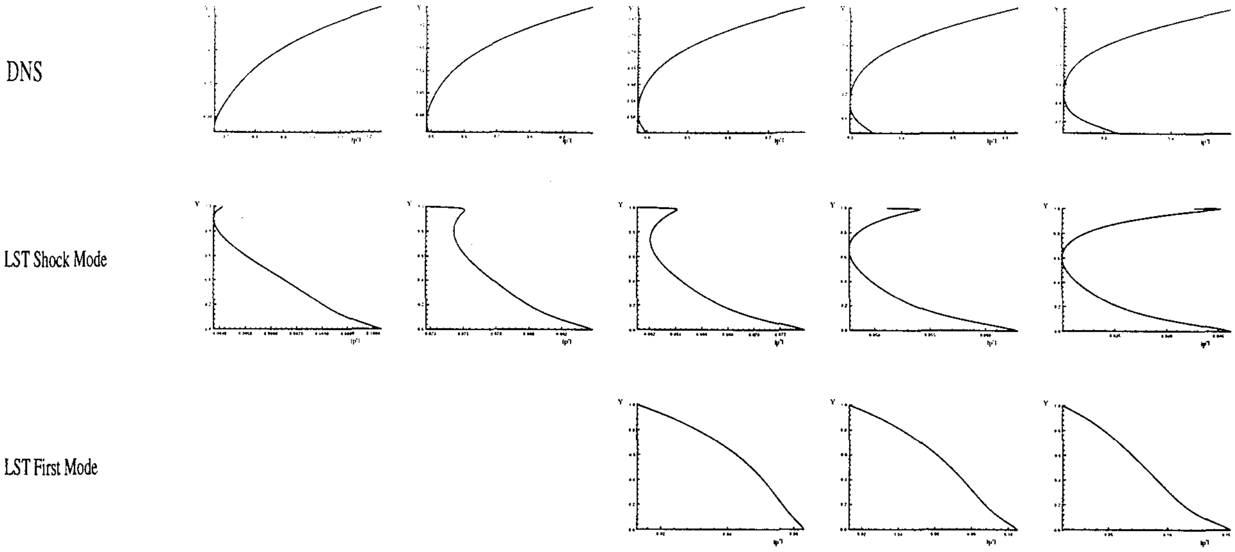

Figure 8: DNS and LST comparison. From left to right, station 1,3,5,7, 9, R from 34.15 to 97.78. Top row, DNS. Second row, shock modes. Third row, first modes. The firse modes in station 1 and 3 are not shown because they are very stable comparing to DNS and shock modes.

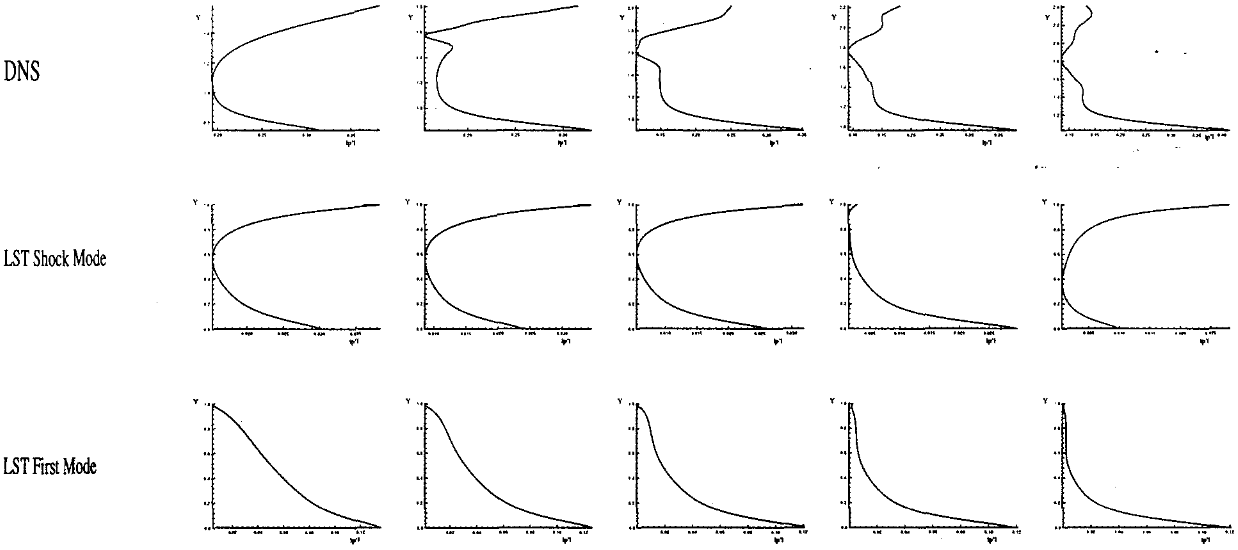

Figure 9: DNS and LST comparison. From left to right, station 11,13,15,17, 19, R from 118.14 to 179.38. Top row, DNS. Second row, shock modes. Third row, first modes.

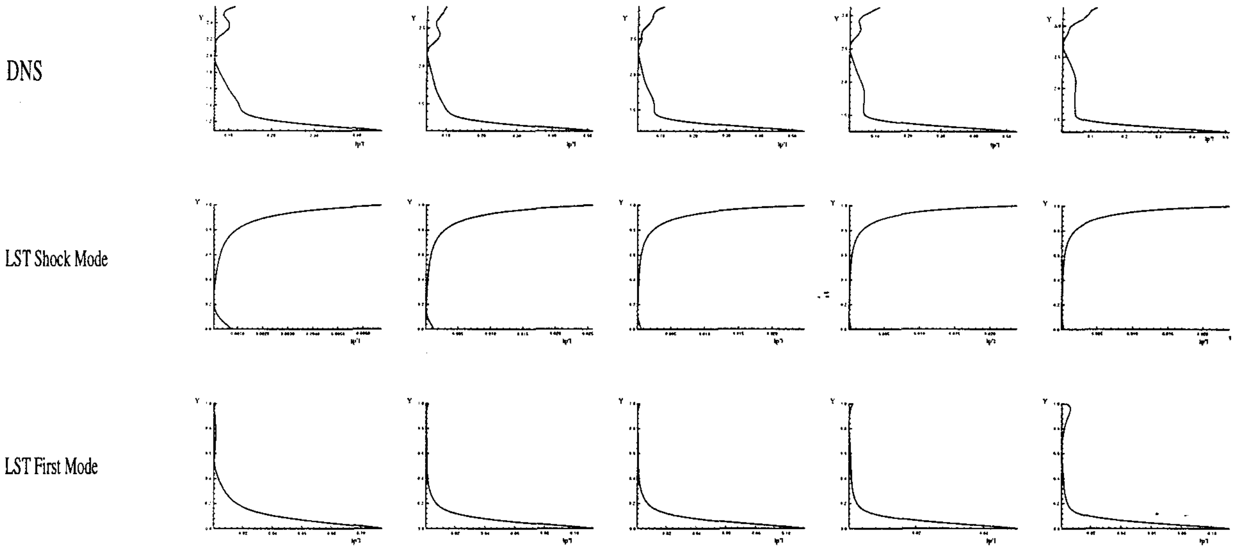

Figure 10: DNS and LST comparison. From left to right, station 21,23,25,27,29, R from 192.54 to 239.74. Top row, DNS. Second row, shock modes. Third row, first modes.

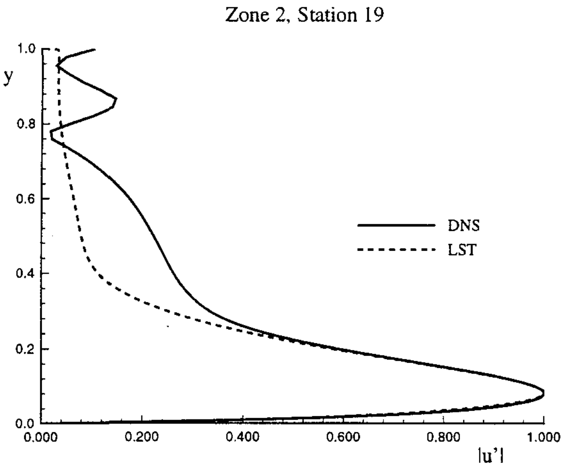

Figure 11: The magnitude of streamwise velocity disturbance from DNS comparing with the LST first mode at Station 19. $R = 179.38, F = 531$.

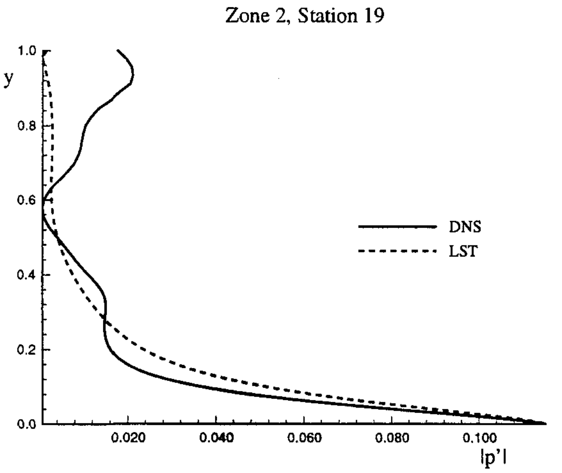

Figure 12: The magnitude of pressure disturbance from DNS comparing with the LST first mode at Station 19. $R = 179.38, F = 531$.

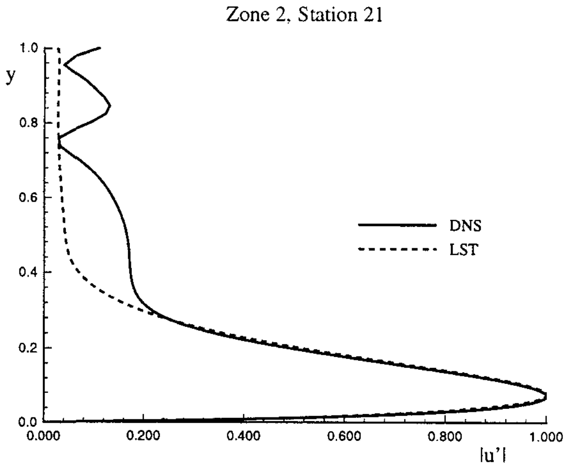

Figure 13: The magnitude of streamwise velocity disturbance from DNS comparing with the LST first mode at Station 21 $R = 192.54, F = 531$.

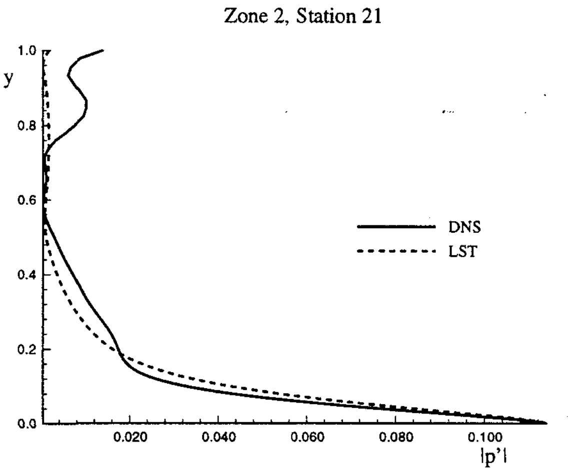

Figure 14: The magnitude of pressure disturbance from DNS comparing with the LST shock mode at Station 21 $R = 192.54, F = 531$.

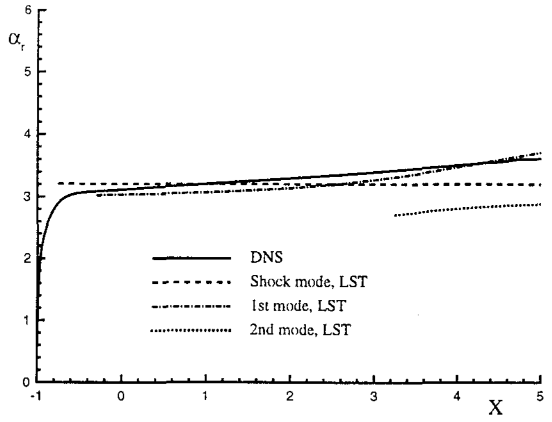

Figure 15: Spatial wavenumber comparison between DNS and LST results. The wavenumber is nondimensionalized by the free stream length scale $0.1m$. F=531.

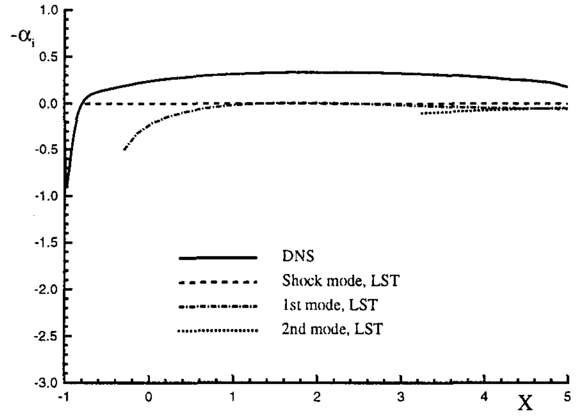

Figure 16: Amplification rate comparison between DNS and LST results. The wavenumber is nondimensionalized by the free stream length scale $0.1m$. F=531.

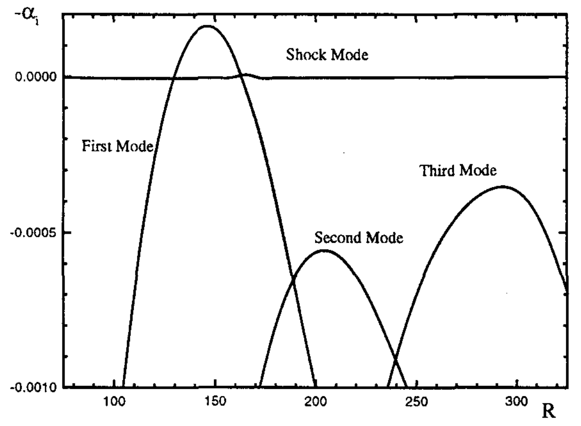

Figure 17: Amplification rate path of LST modes. The reference length scale is the local length scale δ. F=531.

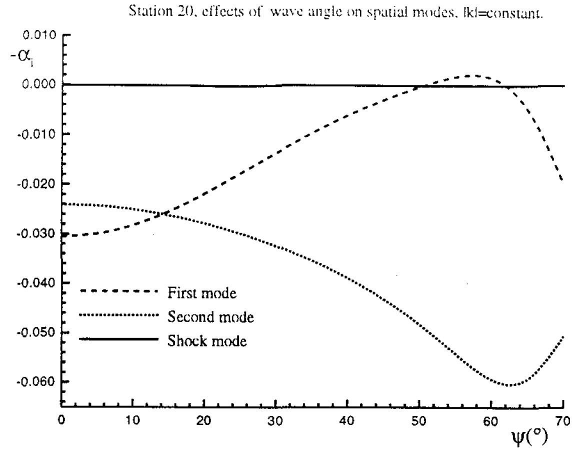

Figure 18: Effects of wave angle on spatial modes with constant $|k|$. F=531. At Station 21, $R = 192.537$.

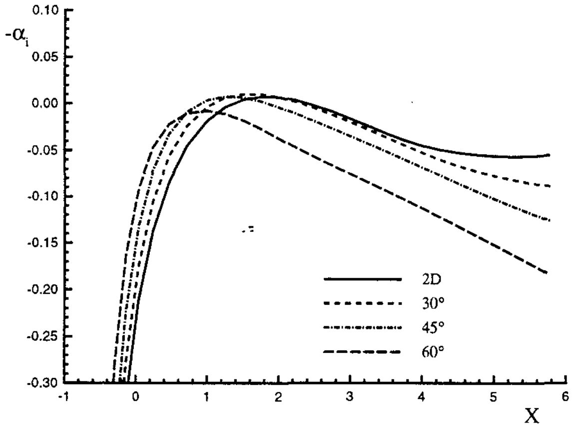

Figure 19: Amplification rate path of first mode waves with different wave angles. F=531. α_i is nondimensionalized by the freestream length scale.

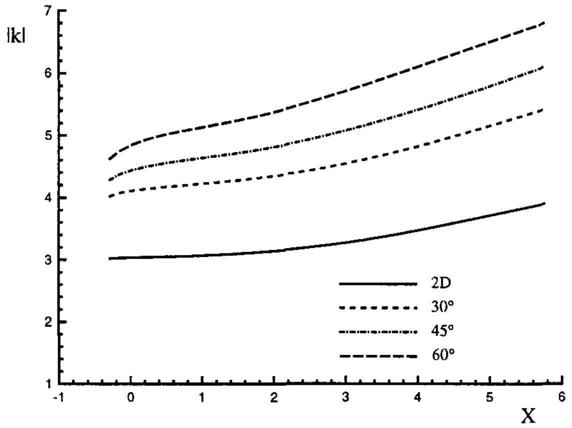

Figure 20: Magnitude of wavenumber vector of first mode waves with different wave angles in the streamwise direction. F=531. The reference length scale is the freestream length scale.

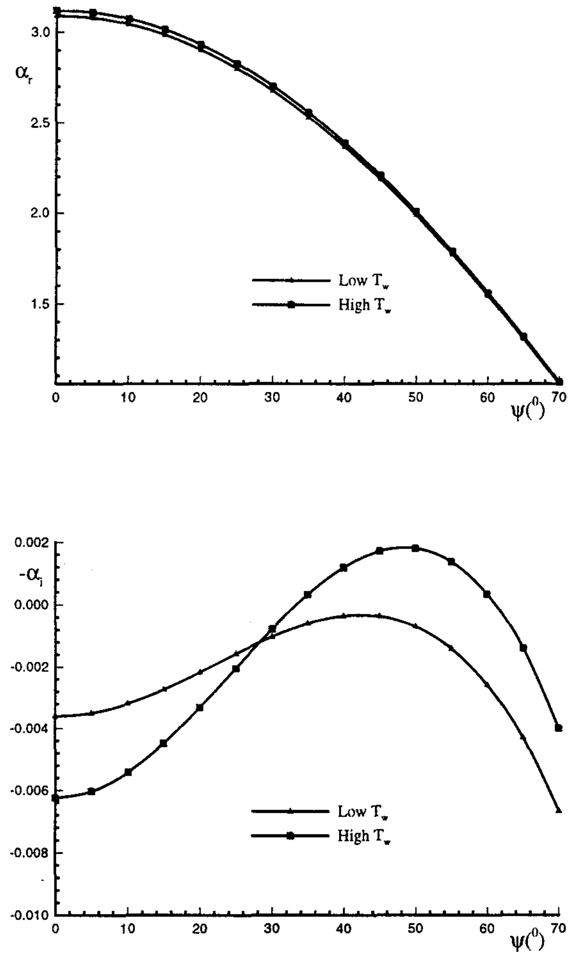

Figure 21: Effects of wall-cooling on 3D first modes. F=531. Upper figure, effects on wavenumber. Lower figure, effects on amplification rate. $l = 0.1m$.

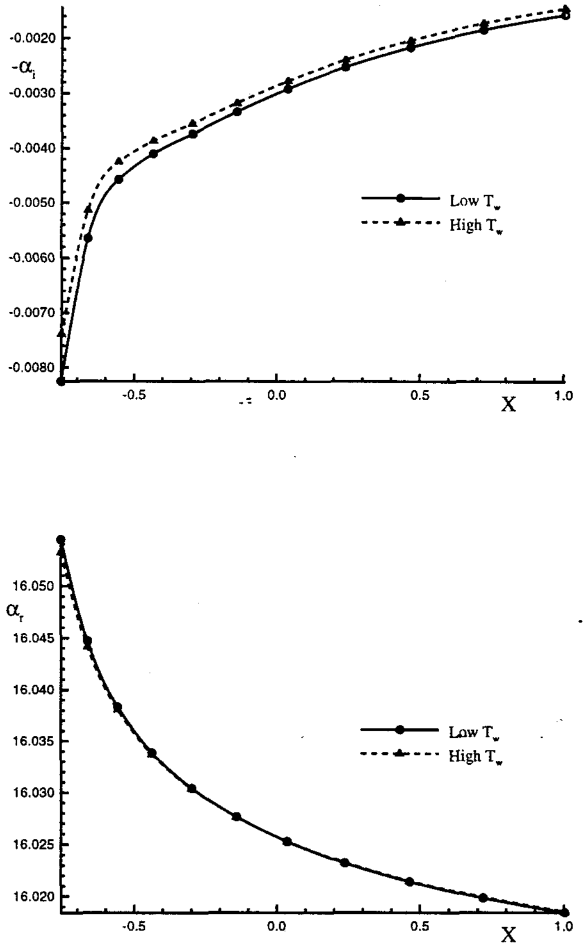

Figure 22: Effects of wall-cooling on shock mode along the streamwise diretion. F=531. Upper figure, effects on wavenumber. Lower figure, effects on amplification rate. $l = 0.1m$.

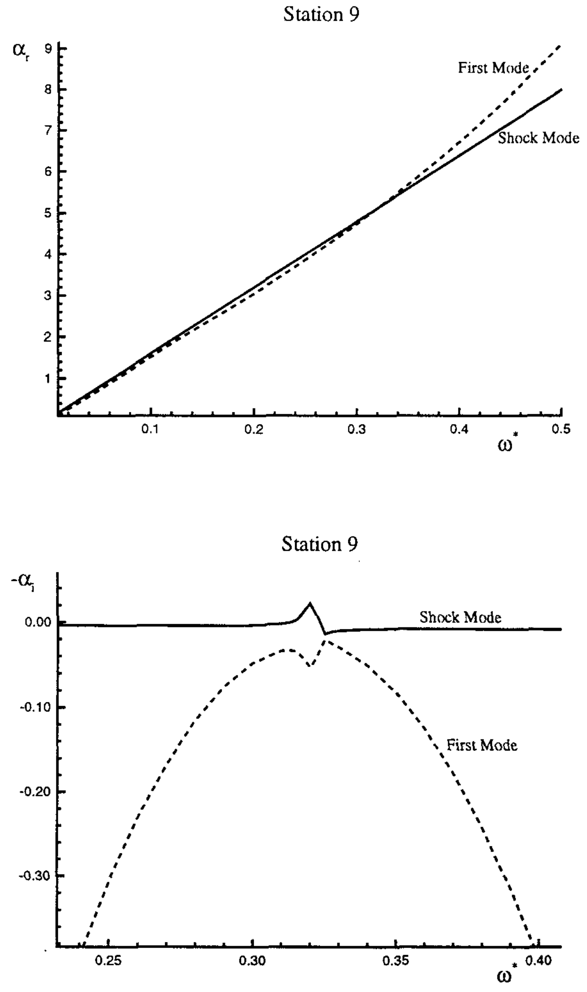

Figure 23: The behavior of the shock mode and first mode with different forcing frequency (normalized by the maximum forcing frequency used in the computation) at station 9. $R = 97.78$. Upper figure, α_r. Lower figure, $-\alpha_i$. $l = 0.1m$.

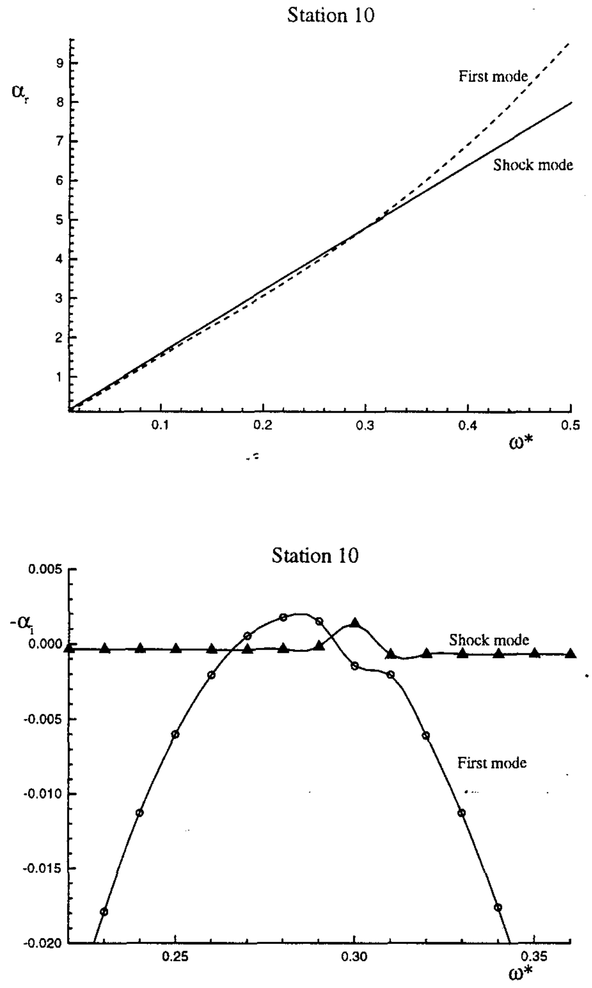

Figure 24: The behavior of the shock mode and first mode with different forcing frequency (normalized by the maximum forcing frequency used in the computation) at station 10. $R = 107.70$. Upper figure, α_r. Lower figure, $-\alpha_i$. $l = 0.1m$.

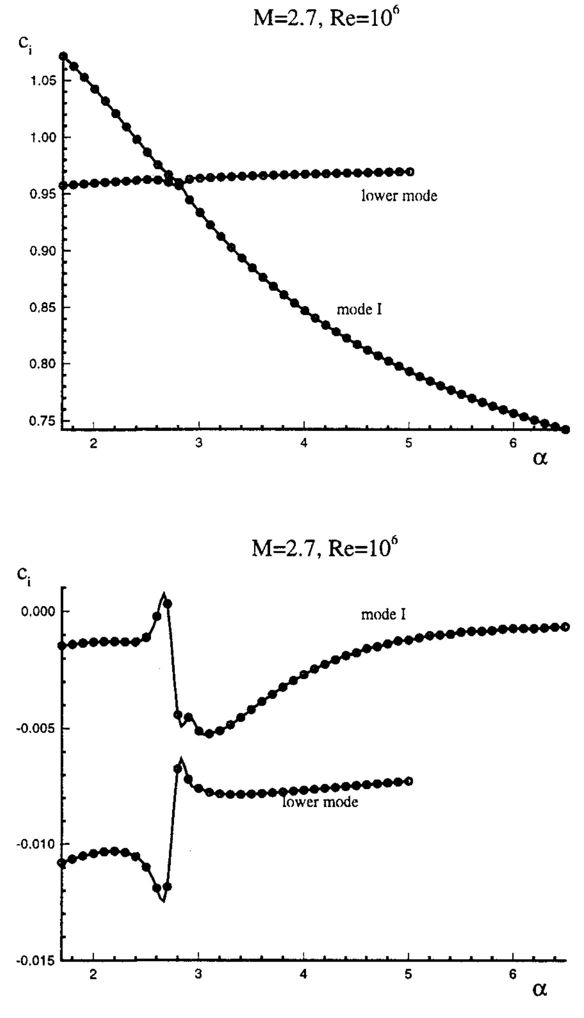

Figure 25: The behavior of temporal amplification rate of Couette flow Mode I when its phase velocity cross with a viscous (lower) mode. Temporal instability. $Re = 10^6, M = 2.7$. Upper figure, $c_r vs. \alpha$. Lower figure, $c_i vs. \alpha$.

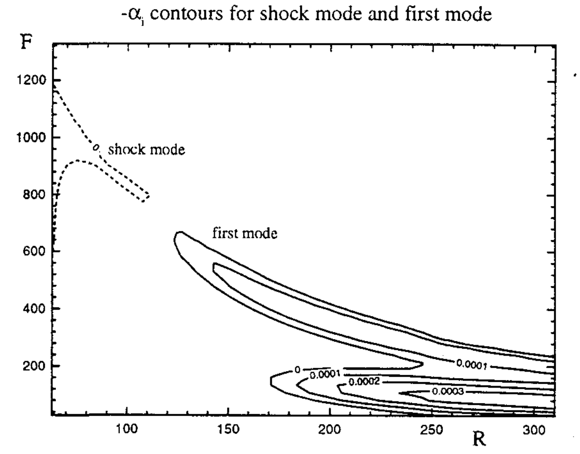

Figure 26: Instability contours at F=531 for the shock mode and the first mode. The characteristic length scale is the local δ.

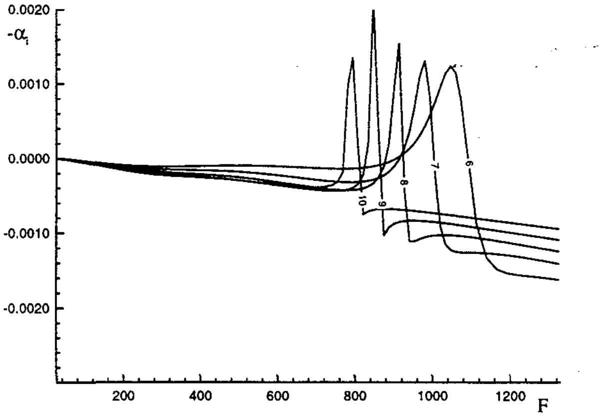

Figure 27: The effects of forcing frequency on the shock mode amplification rate at F=531 at various stations. The characteristic length scale is the local δ.

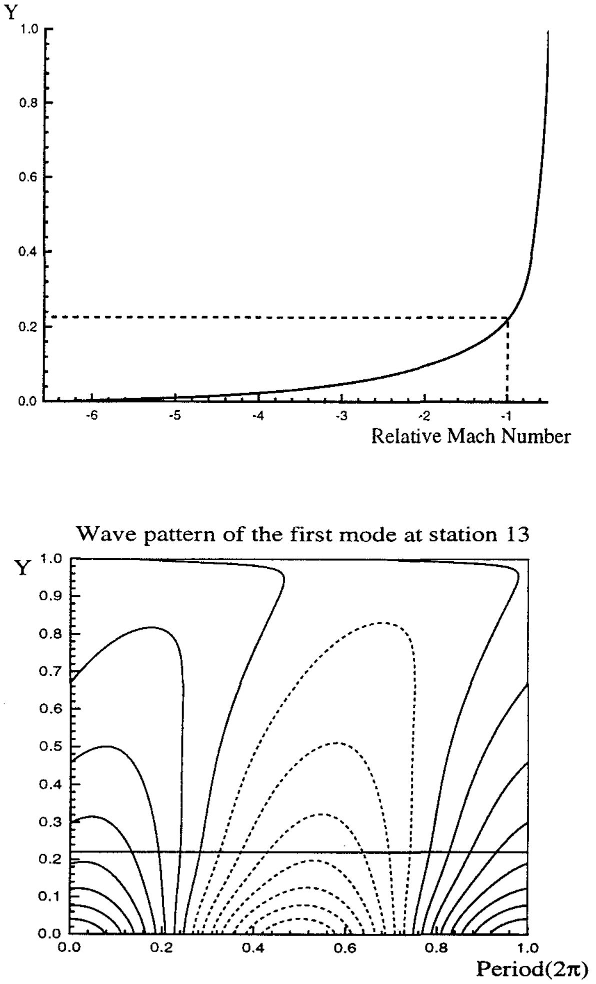

Figure 28: Upper figure, the relative Mach number profile for the first mode. Lower figure, the first mode wave pattern with the sonic line. Location is station 13 with $R = 135.02, F = 531$.

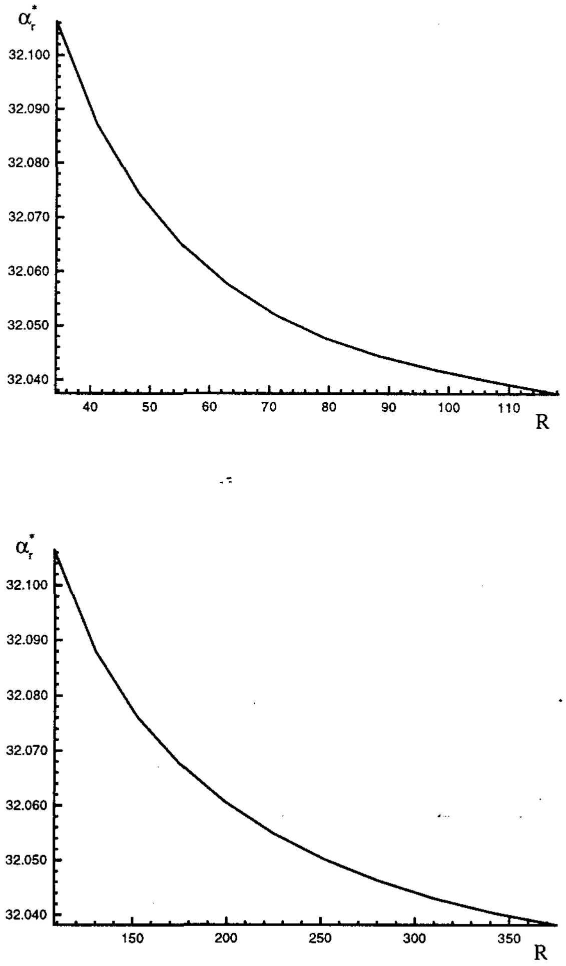

Figure 29: The effects of higher Reynolds number on the shock mode wave number at F=531 at various stations. Upper figure, low Reynolds number case. Lower figure, high Reynolds number case.

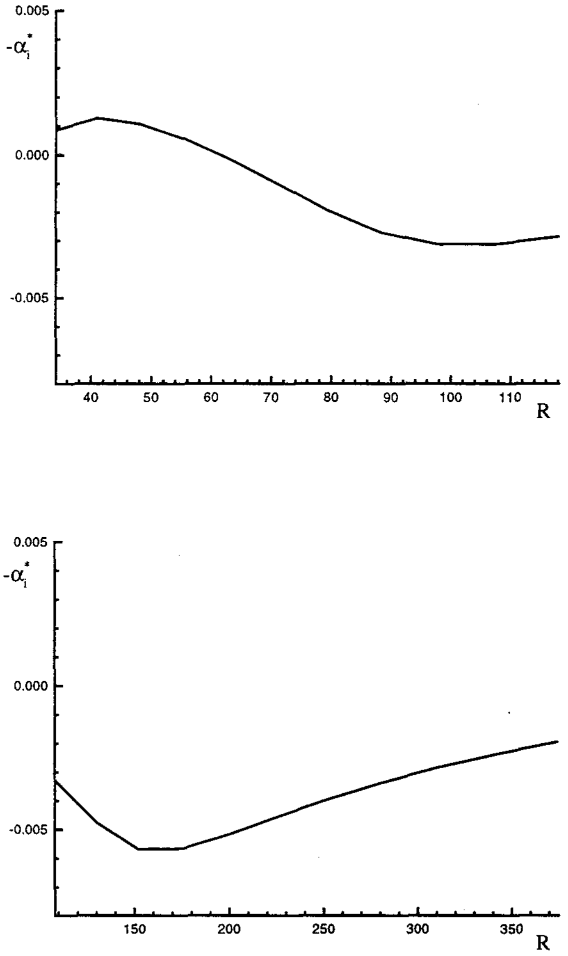

Figure 30: The effects of higher Reynolds number on the shock mode amplification rate at F=531 at various stations.Upper figure, low Reynolds number case. Lower figure, high Reynolds number case.

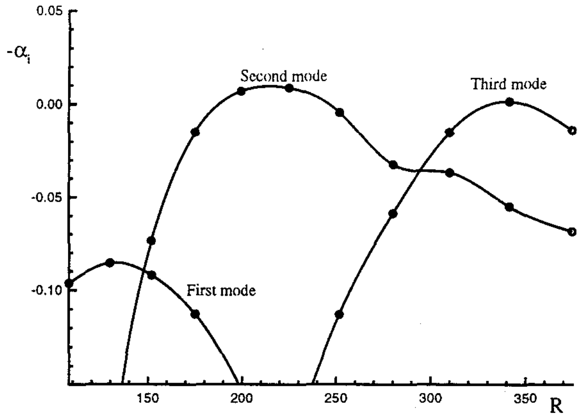

Figure 31: The effects of higher Reynolds number on the amplification rate of dominant boundary layer modes at F=531 at various stations. The characteristic length scale is $1m$ respectively.

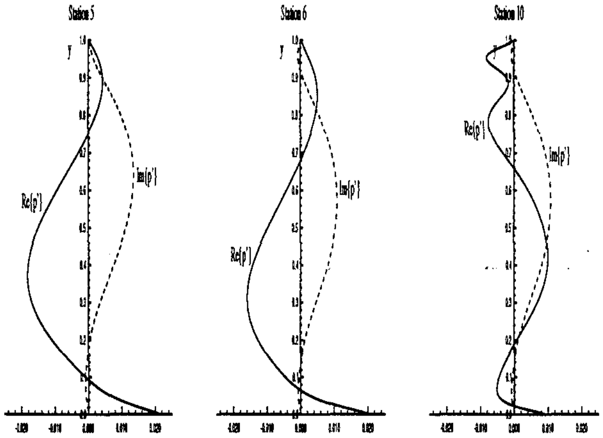

Figure 32: The effects of higher Reynolds number on the amplification rate of dominant boundary layer modes at F=531 at various stations. From left to the right, station 5, station 6 and station 10. The characteristic length scale is $1m$ respectively.